

A Sub-2% Distance to M31 from Photometrically Homogeneous Near-infrared Cepheid Period–Luminosity Relations Measured with the Hubble Space Telescope

Siyang Li¹ , Adam G. Riess^{1,2} , Michael P. Busch¹ , Stefano Casertano², Lucas M. Macri³ , and Wenlong Yuan¹ 

¹ Department of Physics and Astronomy, Johns Hopkins University, Baltimore, MD 21218, USA; sli185@jhu.edu

² Space Telescope Science Institute, 3700 San Martin Drive, Baltimore, MD 21218, USA

³ Department of Physics and Astronomy, Texas A & M University, College Station, TX 77845, USA

Received 2021 June 8; revised 2021 July 13; accepted 2021 July 15; published 2021 October 18

Abstract

We present period–luminosity relations (PLRs) for 55 Cepheids in M31 with periods ranging from 4 to 78 days observed with the Hubble Space Telescope using the same three-band photometric system recently used to calibrate their luminosities. Images were taken with the Wide Field Camera 3 in two optical filters (F555W and F814W) and one near-infrared filter (F160W) using the Drift and Shift (DASH) mode of operation to significantly reduce overheads and observe widely separated Cepheids in a single orbit. We include additional F160W epochs for each Cepheid from the Panchromatic Hubble Andromeda Treasury and use light curves from the Panoramic Survey Telescope and Rapid Response System of the Andromeda galaxy project to determine mean magnitudes. Combined with a 1.28% absolute calibration of Cepheid PLRs in the Large Magellanic Cloud from Riess et al. in the same three filters, we find a distance modulus to M31 of $\mu_0 = 24.407 \pm 0.032$, corresponding to 761 ± 11 kpc and 1.49% uncertainty including all error sources, the most precise determination of its distance to date. We compare our results to past measurements using Cepheids and the tip of the red giant branch. This study also provides the groundwork for turning M31 into a precision anchor galaxy in the cosmic distance ladder to measure the Hubble constant together with efforts to measure a fully geometric distance to M31.

Unified Astronomy Thesaurus concepts: Cepheid variable stars (218); Galaxies (573); Cepheid distance (217); Cosmology (343); Observational astronomy (1145); Observational cosmology (1146); Hubble Space Telescope (761); Near infrared astronomy (1093); Optical astronomy (1776)

Supporting material: machine-readable tables

1. Introduction

Cepheids are variable giant stars that lie in the instability strip of the Hertzsprung–Russell diagram. They pulsate in a periodic expansion and contraction, oscillations that overshoot their hydrostatic equilibrium points due to the temperature dependence of their atmospheric opacity. The timescale of these pulsations is proportional to a star’s density, which is a function of mass and luminosity. The resulting period–luminosity relations (PLRs; Leavitt & Pickering 1912) and the great luminosities of Cepheids allow them to be used as standard candles to determine extragalactic distances. By first using high-precision geometric distance measurements to calibrate nearby Cepheids in galaxies such as the Milky Way (MW) or the Large Magellanic Cloud (LMC), the relative apparent magnitudes between nearby and more distant Cepheids can be used to determine absolute distances. In particular, Cepheids play a crucial role in the cosmic distance ladder used to measure the Hubble constant, H_0 , because they can be combined with other standard candles such as Type Ia supernovae to determine distances to further galaxies in the Hubble–Lemaître flow (Riess et al. 2016).

The Andromeda galaxy (M31, NGC 224) is the nearest spiral to our own, and together with its Cepheid variable V1 it played a prominent role in establishing the distance scale of the universe (Hubble 1929). Due to its proximity, M31 could serve as an anchor in the cosmic distance ladder. However, the lack of a

robust geometric calibration, and the relatively high inclination and accompanying extinction, has historically made it difficult to reduce the uncertainty in its distance measurements. Blending has been shown to bias ground-based observations by up to 0.2 mag (Mochéjska et al. 2000; Vilardell et al. 2007), and both crowding and differential extinction cause high dispersion in the Cepheid PLR. While past studies (Macri et al. 2001; Riess et al. 2012; Wagner-Kaiser et al. 2015; Kodric et al. 2018b) have shown that space-based observations can help reduce the effects of crowding and blending, inhomogeneities between the filter systems used to observe Cepheids in M31 and their geometric calibrations yielded uncertainties in the distance measurements of between 3% and 5%, limiting our knowledge of the distance to M31 and studies that use M31 to calibrate stellar luminosities.

M31 is also an ideal laboratory to investigate differences among different methods of distance measurement. Recent measurements of H_0 using Cepheid and tip of the red giant branch (TRGB) methods yield mildly different results that could be due to chance or differences in calibration (Freedman et al. 2019; Riess et al. 2021). Comparing a high-precision Cepheid measurement to M31 to past TRGB measurements along with other hosts in common may help clarify whether this difference is caused by chance, differences in calibration, or differences in environments.

Previously, the large observatory overheads and narrow field of view (FOV) of the Hubble Space Telescope (HST) limited the possibility of observing a large number of Cepheids in M31 in the same three filters as Riess et al. (2019a), who recently established a high-precision Cepheid anchor in the LMC based on a robust geometric distance estimate (Pietrzynski et al. 2019). The



Original content from this work may be used under the terms of the [Creative Commons Attribution 4.0 licence](https://creativecommons.org/licenses/by/4.0/). Any further distribution of this work must maintain attribution to the author(s) and the title of the work, journal citation and DOI.

availability of the Drift and Shift (DASH; Momcheva et al. 2017) mode of observing starting from Cycle 24 in 2016 allowed us to circumvent these obstacles and observe a greater number of Cepheids (up to 12 Cepheids in three filters in one orbit). DASH uses HST gyroscopes for guiding and is advantageous for our short integrations of 10–21 s, allowing us to eliminate the 6 minutes overhead for acquisition of each guide star required for slews beyond 2' under Fine Guidance Sensor (FGS) control. We further used subarray observations to reduce additional overheads that would otherwise require a 350 s memory buffer dump for each full UVIS frame. The expected gyro drift was $\sim 0.^{\circ}002$ per second, smaller over each exposure than the $0.^{\circ}04$ and $0.^{\circ}128$ pixels for WFC-UVIS and WFC3-IR, respectively. Further advantages of the DASH mode for observing Cepheids are described in Riess et al. (2019a). For each Cepheid we made two observations separated by a week to improve precision and to test the expected phase of the Cepheid.

To augment the number of F160W epochs, we drew upon frames from the Panchromatic Hubble Andromeda Treasury (PHAT) (PI: J. Dalcanton). PHAT is an HST multi-cycle program that resolved more than 100 million stars in a third of the star-forming disk in M31 using six filters (F275W, F336W, F475W, F814W, F110W, and F160W) ranging from the ultraviolet to near-infrared (Dalcanton et al. 2012). We only used the PHAT F160W measurements since the UV/optical observations were obtained with a different camera (ACS). Due to the relatively small amplitudes of Cepheid light curves in the near-infrared, the F160W magnitudes at random-phase observations from PHAT are on average close to those at mean phase (Madore & Freedman 1991). As PHAT uses the same F160W filter as used in Riess et al. (2019a) and this study, we can use PHAT images to further increase the number of epochs in F160W and obtain a better estimate of the mean magnitude for each phase-corrected Cepheid. The Panoramic Survey Telescope and Rapid Response System (Pan-STARRS1) survey of the Andromeda galaxy (PAndromeda) obtained light curves for 2686 Cepheids in the *gri* bands. Combined with random-phase observations of corresponding HST Cepheids, the mean magnitude estimations for the Cepheids can be improved using these light curves and previously constructed templates (Yoachim et al. 2009; Inno et al. 2015).

In this study, we use phase-corrected PLRs from multi-epoch HST observations of 55 M31 Cepheids and a calibration to the LMC that uses the same photometric system and instrument to reduce the uncertainty in the distance to M31 to 1.49%. In Section 2, we describe the measurement and photometry of the Cepheids analyzed in this study. In Section 3, we construct PLRs in F555W, F814W, F160W, and both visible (VIS) and near-infrared (NIR) Wesenheit indices, and in Section 4 we use the NIR Wesenheit PLR to derive a distance to M31, compare our result with those in past literature, and discuss the potential use of M31 as a new anchor galaxy. Finally, in Section 5, we discuss the implications of our results.

2. M31 Cepheid Standards

2.1. DASHing through M31

We obtained multi-epoch HST images of 57 Cepheids in M31 in two WFC3-UVIS optical filters (F555W and F814W) and one WFC3-IR near-infrared filter (F160W) as part of program GO-15146 (PI: Riess) using DASH. Exposure times were 10 s for F555W and F814W and 21.3 s for F160W. We

intended to obtain two epochs per filter for each Cepheid, but HST Gyro 2 experienced severe degradation during our observations, resulting in sporadic and unpredictable drift—in some cases exceeding its expected value by more than an order of magnitude. Characterization of this degradation can be found in Riess et al. (2019a). As a result, 45 out of the 392 images obtained were unusable, leaving 55 Cepheids for analysis.

Figure 1 shows the locations of these Cepheids within M31, while Table 1 lists the following properties: (1) target ID, (2) corresponding frame, (3) filter, (4) date of observation, (5) exposure time, (6) image *X* coordinates, (7) image *Y* coordinates, (8) corresponding program (GO-15146 or PHAT), and (9) image removal flag (described in the table footnote).

We removed CEPH-11.01715+41.46200 and CEPH-11.21898+41.47505 from further consideration due to flag 4 (see Table 1), and further determined that two Cepheids in GRP-11.09581+41.35417 ($P = 36.106, 36.154$ days) and two Cepheids in GRP-11.29561+41.60411 ($P = 48.447, 48.472$ days) were the same object. For each of these two Cepheids, we combine their measurements and take the average of the two periods for each pair in our analysis. The final sample consists of 55 unique variables.

2.2. Photometry

We retrieved calibrated frames using the Mikulski Archive for Space Telescopes (MAST) website: *flc* suffix for the optical images, corrected for charge transfer efficiency, and *flt* suffix for the near-infrared ones. The goal of GO-15146 was to obtain two epochs in each filter for each Cepheid separated by one week to increase the accuracy of the mean magnitude recovered using template-fitting (described in Section 2.3 below). We used ground-based *r*-band light curves from PAndromeda (Kodric et al. 2018a) for phase corrections, since that band had the greatest number of epochs and frames per epoch on average available for each Cepheid. We find an average of 319 epochs per Cepheid for the PAndromeda light curves used in this study. We created three samples of Cepheids: “gold,” “silver,” and “gold+silver.” The gold sample consists of 42 Cepheids having *r*-band light curves from PAndromeda that can be used for phase corrections. The silver sample consists of 13 Cepheids that either do not have corresponding light curves or had light curves rejected by Kodric et al. (2018a) using a color cut. In the silver sample we adopt an unweighted average of the epoch magnitudes of each Cepheid to avoid bias that would be caused by higher statistical uncertainties in fainter Cepheids as well as the larger uncertainty due to their random phase. The gold+silver sample combines the gold and silver samples.

Because the use of DASH resulted in an inaccurate World Coordinate System for each GO-15146 image, we first located Cepheids using the algorithm from Riess et al. (2019a) and centered the Cepheid using DAOStarFinder from the *photutils* package in Python (Bradley et al. 2020). We measured all magnitudes using aperture photometry with PythonPhot, which uses the DAOPHOT routines (Stetson 1987) translated into Python by Jones et al. (2015). Aperture photometry, with radii much larger than the point-spread function (PSF) FWHM and the measured field drift, is advantageous over PSF fitting for the frames used in this study because it is less sensitive to the broadening of the PSF that could result from gyroscopic

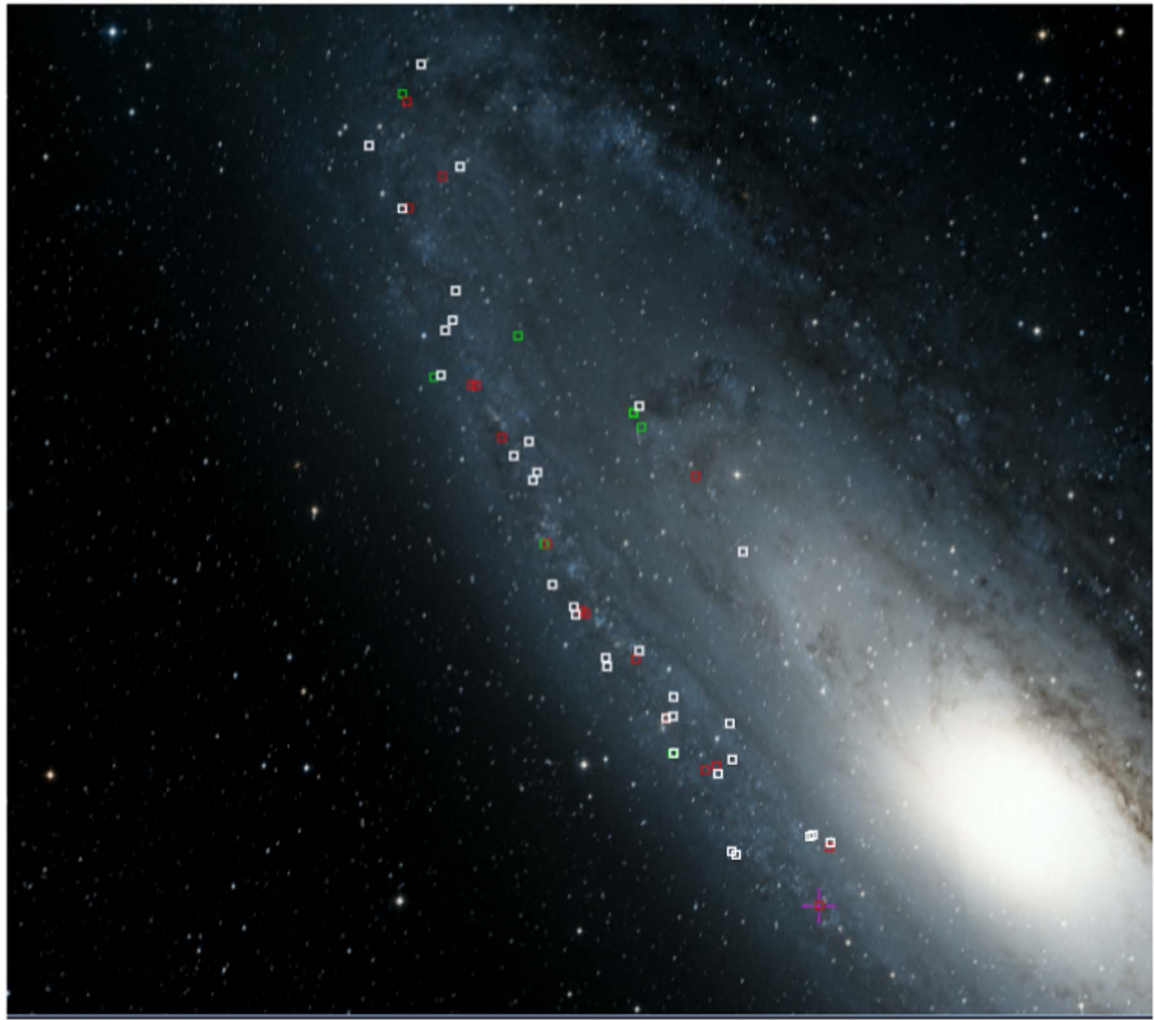


Figure 1. Locations of the 55 Cepheids analyzed in this study. Mean magnitudes residuals of $e \geq 0.5$, $-0.5 < e < 0.5$, and $e \leq -0.5$ using the F555W PLR fit from Riess et al. (2019a) are shown in red, white, and green, respectively. Image generated using AstroView in the Mikulski Archive for Space Telescopes website.

drift. This drift was measured from the change in the positions of the intended targets between successive images.

We multiplied each frame by a pixel area map, provided by STScI, corresponding to the respective camera and position of the subarray. The pixel area maps are used to correct for the photometric impact of the flat-fielding process in the CALWF3 pipeline on pixels of nonuniform size. We set the aperture radii to 3 pixels ($\sim 0''.12$) for WFC3-UVIS images and 2 pixels ($\sim 0''.25$) for WFC3-IR images. While smaller aperture radii can increase the nominal signal-to-noise ratio, they also increase sensitivity to PSF broadening. We selected these aperture radii to balance these two effects, as well as to reduce contamination from nearby stars or cosmic rays. We tested for potential errors from large drifts, flagging and removal of cases where the error was not negligible.

For images taken in F555W, we applied a zero-point of 25.727 mag (Vega system) and an aperture correction of -0.183 mag from a 3 pixel radius to infinity. For images taken in F814W, we applied a zero-point of 24.581 mag and an aperture correction of -0.272 mag from a 3 pixel radius to infinity. These values are consistent with those used by Riess et al. (2019a) for LMC Cepheids. For images taken in F160W, we applied a zero-point of 24.71 mag and the same aperture correction of -0.200 mag from a 3 pixel radius to infinity

derived by Riess et al. (2019a), combined with a -0.166 mag correction from a 2 pixel to a 3 pixel radius for a total aperture correction of -0.366 mag from a 2 pixel radius to infinity. Although this zero-point may differ by ~ 0.02 mag from the latest or future STScI calibrations or from small WFC3-IR sensitivity variations over time (Kozhurina-Platais & Baggett 2020), we used the same values used in Riess et al. (2019a) to nullify zero-point errors through the comparison to LMC Cepheids.

In a few cases, visual inspection indicated the presence of significant crowding near the target Cepheid. For these objects, we used smaller aperture radii of 2 pixels for F555W and F814W images and 1 pixel for F160W images, along with corresponding aperture corrections to infinity of -0.450 , -0.500 , and -0.944 mag. Although applying such smaller apertures decreases the signal-to-noise ratio, it further reduces contamination from nearby stars that would bias our photometry for these particular targets.

2.3. Phase Corrections

We estimate the mean magnitude for each Cepheid in the gold sample from our random multi-epoch observations by applying phase corrections using periods and ground-based light curves from PAndromeda (Kodric et al. 2018a). Using PAndromeda light

Table 1
Observations of M31 Cepheids

Target (1)	Frame (idit) (2)	Filter (3)	MJD (4)	Exp. Time (s) (5)	X (6)	Y (7)	Program (8)	Flag (9)
GRP-11.20822+41.44917	510sbq	F555W	58135.23621	10.0	897.7	471.0	GO-15146	
...	510scq	F814W	58135.23765	10.0	889.7	469.7	GO-15146	
...	510spq	F160W	58135.25567	21.3	392.3	274.9	GO-15146	
GRP-11.24332+41.50926	508g0q	F555W	58103.65339	10.0	746.0	518.9	GO-15146	
...	507rlq	F814W	58097.56431	10.0	711.2	523.97	GO-15146	

Note. Description of flags for column 9: (1) excessive drift, PSF semimajor axis greater than 3 pixels for F555W and F814W and 2 pixels for F160W; (2) Cepheid is not fully in frame; (3) Cepheid matching algorithm from Riess et al. 2019a has fewer than 10 matches and the Cepheid could not be found visually; (4) Cepheid removed because all images in one or more filters were unrecoverable due to flags 1–3.

(This table is available in its entirety in machine-readable form.)

curves to estimate mean magnitudes for the gold-sample Cepheids results in lower uncertainties than for silver-sample Cepheids, which use an unweighted mean for the magnitude estimate. The additional information provided by the PAndromeda light curves allows us to infer the amplitude and phase of the gold-sample Cepheids, which is not possible for the silver sample. Figure 2 shows examples of template fits for four Cepheids. We use V - and I -band templates from Yoachim et al. (2009) and H -band templates from Inno et al. (2015) and approximate the V , I , and H bands as F555W, F814W, and F160W, respectively. The uncertainties in the color terms used to transform between the HST and Johnson–Cousins filter systems are negligible. Riess et al. (2019a) find that a 10% error in the color term would change the transformed magnitudes by less than 0.1 mmag. The procedure we use fits templates to measurements simultaneously in all three filters and has five free parameters: phase, V -band amplitude, and three mean magnitudes. We fix the ratio between the H - and V -band amplitudes to 0.34 for $P \leq 20$ days and 0.40 for $P > 20$ days following Inno et al. (2015), and the ratio between I - and V -band amplitudes to 0.58 following Yoachim et al. (2009). Using a single H -to- V amplitude ratio of 0.40 mag does not change the final distance. The template-fitting procedure performs a two-parameter grid search through phase and V -band amplitude and estimates a mean magnitude correction for each filter using the Modified Julian Date, period, phase, and amplitude at each iteration. This correction is added to the HST epochs and is not a function of magnitude and so is constant for a given combination of period, filter, phase, and amplitude. This correction is then added to each epoch to estimate the mean magnitude, and if there is more than one epoch for a given filter, we take a weighted average of the estimated mean magnitudes using the photometric errors as weights. For each iteration through the grid search, χ^2 is computed for all three filters and V -band amplitude with the estimated mean magnitudes used as the expected value and the HST epochs used as the actual value in the χ^2 terms. As the V -band amplitudes and phases are free parameters, the χ^2 minimization procedure allows for the template fits to account for possible light-curve variations. We use the mean magnitudes corresponding to the minimum χ^2 as the final mean magnitude estimates. The mean phase corrections and standard deviations for the phase corrections for F555W, F814W, and F160W are -0.023 ± 0.210 , -0.011 ± 0.123 , and 0.003 ± 0.070 mag, respectively. Because the phases are free parameters, the phase errors from the PAndromeda light curves do not enter into the final error calculation.

2.4. Wesenheit Indices

We combine our F555W, F814W, and F160W mean magnitude estimates into reddening-free VIS Wesenheit (m_I^W) and NIR Wesenheit (m_H^W) indices (Madore 1982) using the same formulations from Riess et al. (2016, 2019a):

$$m_I^W = m_{F814W} - 1.3(m_{F555W} - m_{F814W})$$

$$m_H^W = m_{F160W} - 0.386(m_{F555W} - m_{F814W}) \quad (1)$$

where 0.386 is derived from Fitzpatrick (1999) and 1.3 is derived from Cardelli et al. (1989), both using $R_V = 3.1$. The Wesenheit indices are useful for reducing dispersion in the PLR caused by differential extinction and the nonzero temperature width of the instability strip (at a fixed period, cooler Cepheids are redder and fainter).

For the gold sample, the final mean magnitude errors for each Cepheid are calculated by adding in quadrature the photometric errors with template errors of 0.05, 0.03, and 0.017 mag for V , I , and H , respectively, from Riess et al. (2019a) and Inno et al. (2015). An intrinsic scatter of 0.069 mag from Riess et al. (2019a) is then added in quadrature to the NIR Wesenheit index after error propagation. For the silver sample, the F555W, F814W, and F160W mean magnitude errors are calculated by adding in quadrature the photometric errors for each epoch and dividing by the square root of the number of epochs used. These errors are propagated into the VIS and NIR Wesenheit indices. We then add a random phase error of 0.13 mag from Macri et al. (2015) in the VIS and NIR Wesenheits in quadrature. A 10% change in this random phase error only changes the final distance modulus by 2 mmag. As with the gold sample, an intrinsic scatter of 0.069 mag is additionally added in quadrature to the NIR Wesenheit index. The mean magnitude uncertainties for F555W, F814W, F160W, m_I^W , and m_H^W after phase corrections are 0.137, 0.113, 0.073, 0.316, and 0.124 mag, respectively, for the gold sample, while for the silver sample they are 0.100, 0.076, 0.042, 0.263, and 0.164 mag, respectively.

2.5. Geometric and Count-rate Nonlinearity Corrections

We applied geometric corrections to account for differences in the distance of each Cepheid from the center of M31, which can be up to a few hundredths of a magnitude. We adopt the same parameters as in Dalcanton et al. (2012): an inclination of $i = 70^\circ$, a position angle of $\theta = 43^\circ$, and a center of $\alpha(2000) = 10.68473$ and $\delta(2000) = 41.26805$. We estimate an

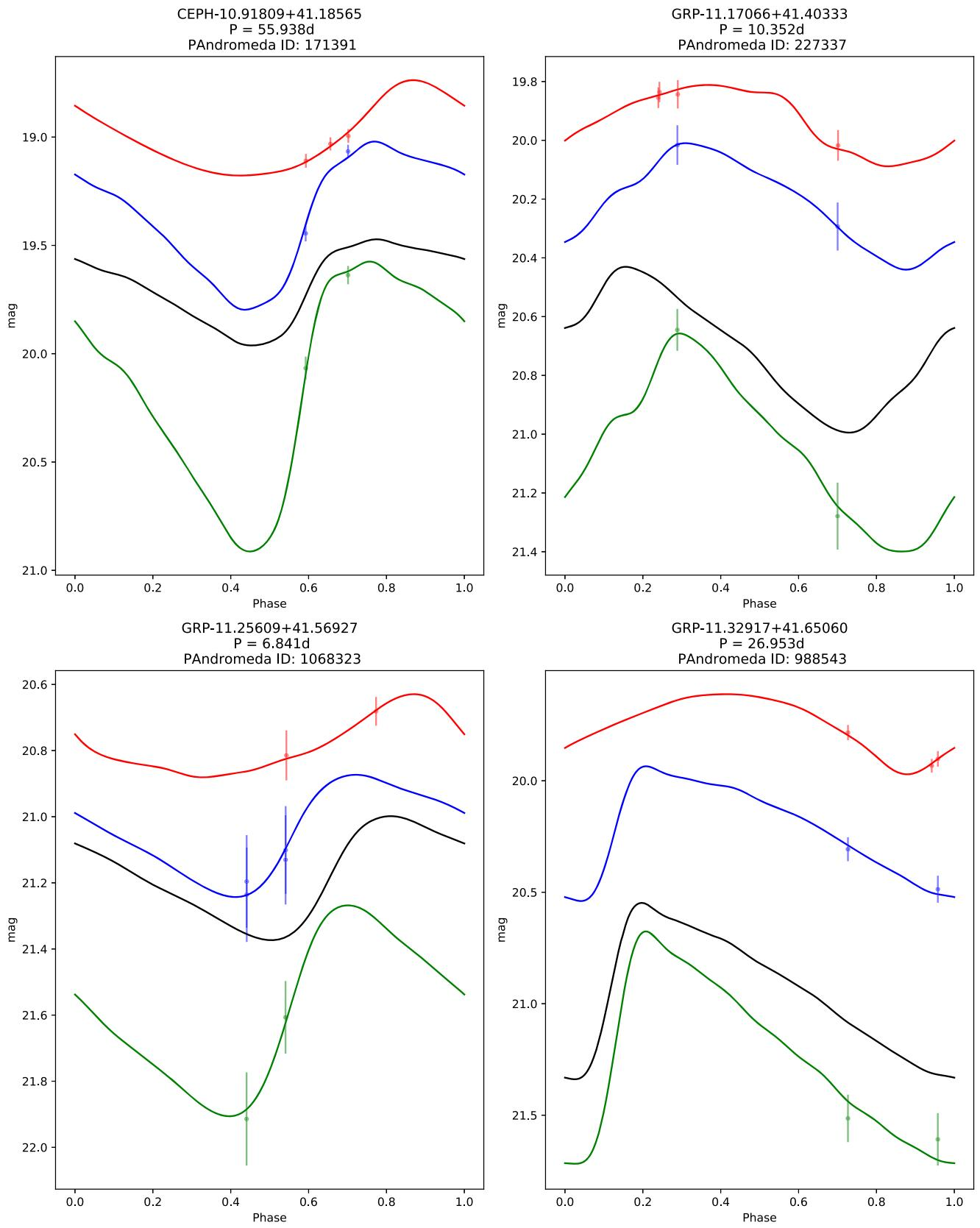


Figure 2. Four example template fits from the gold sample. Black lines correspond to r -band light curves from PAndromeda. Red, blue, and green correspond to F160W, F814W, and F555W, respectively. Dots with error bars represent HST observations and their photometric errors while solid lines represent the template fit. Curves are shifted as follows: upper left: F160W+2, F814W+0.6, F555W-0.7; upper right: F160W+1, F814W+0.2; lower left: F160W+1.2, F814W+0.4, F555W-0.1; lower right: F160W+2, F814W+0.8, F555W-0.2.

error of 0.011 mag for this geometric correction by taking the standard deviation of the mean of corrections using the parameters above plus the four possible combinations of $i = 74^\circ$ from Courteau et al. (2011), $i = 77^\circ$ from Walterbos & Kennicutt (1988), $\theta = 45^\circ$ from Seigar et al. (2008), and $\theta = 38.1^\circ$ from Tempel et al. (2010). This geometric correction is applied to m_I^W and m_H^W , with mean values for the gold and silver samples of 0.011 mag and 0.012 mag, respectively. Mean magnitudes and their geometric corrections for each Cepheid can be found in Table 2. A positive geometric correction corresponds to a Cepheid farther than the center of M31.

We also applied corrections to account for count-rate nonlinearity (CRNL) or reciprocity failure, which dims fainter sources more than brighter ones due to a decreased photon collection efficiency at low count rates compared to high count rates for WFC3-IR. We adopt the CRNL correction of 0.0077 mag dex $^{-1}$ from Riess et al. (2019b). To account for CRNL when using LMC as an anchor, as M31 is fainter than the LMC, the F160W (or equivalently, m_H^W) magnitudes for M31 must contain a correction corresponding to 2 dex in the brighter direction relative to the LMC. This would be equivalent to instead applying the correction so that the LMC has a 2 dex correction in the fainter direction if no correction to M31 were made. As the LMC anchor from Riess et al. (2019a) used to determine the distance to M31 below already accounts for a 4 dex CRNL correction in the fainter direction, we add 0.0154 ± 0.0055 mag to m_H^W so that the LMC has a net 2 dex CRNL correction relative to M31 in the fainter direction.

3. Period-Luminosity Relations

Figure 3 shows PLRs for F555W, F814W, and F160W, while Figure 4 presents PLRs for m_I^W and m_H^W , both for the gold +silver sample. Weighted linear least-squares fit parameters for m_I^W and m_H^W for various samples can be found in Table 3. Column (1) lists the Wesenheit index (m_I^W or m_H^W), (2) corresponding sample, (3) the number of Cepheids in that sample, (4) the dispersion of a two-parameter weighted linear least-squares fit not accounting for intrinsic scatter, (5) the slope for the two-parameter fit with its error in parentheses, (6) the intercept for the two-parameter fit with its error in parentheses, (7) χ^2 per degree of freedom, χ^2_{dof} , for the two-parameter fit, (8) the intercept for a weighted linear least-squares fit with fixed slopes of -3.31 for m_I^W and -3.26 for m_H^W (Riess et al. 2019a) with its error in parenthesis, and (9) χ^2_{dof} for the fixed-slope fit. One Cepheid (CEPH-11.12919 +41.61338) in the gold sample deviates from the m_H^W PLR fit beyond the value allowed by Chauvenet's criterion. We denote the sample without this object as gold+silver-1 and find small improvements in the resulting fits.

We attribute the differences in F555W, F814W, and F160W slopes compared to those in other studies (Wagner-Kaiser et al. 2015; Kodric et al. 2018a; Riess et al. 2019a) to the effects of high differential extinction in M31. In Figure 1, we color the locations of the target Cepheids using red, white, and green for mean-magnitude residuals of $e \leq -0.5$, $-0.5 < e < 0.5$, and $e \geq 0.5$ when compared to the F555W PLR fit from Riess et al. (2019a), respectively. Riess et al. (2011) noted that young, long-period Cepheids tend to be concentrated in the spiral arms of their host galaxy where the bulk of star formation occurs, while older, short-period Cepheids do not have a preferential spatial distribution. As the spiral arms contain a higher amount of dust than the inner portions of the disk and bulge when viewing a galaxy with high

inclination such as M31 ($\sim 75^\circ$), long-period Cepheids in the spiral arms suffer on average from more extinction than shorter-period Cepheids. As a result, the long-period side of the PLR fit is pushed faintward more so than than the short-period side, with the relative difference dependent on the distribution of Cepheids in a given sample. The high inclination of M31 increases all extinction effects, and the increase in the difference is likely a natural consequence of this. As observations in the near infrared are less affected by extinction, we see that there is less of a difference between the F160W slopes from this study, Wagner-Kaiser et al. (2015), and Kodric et al. (2018a), and the m_H^W between this study and Riess et al. (2019a). We find a mean reddening $R_V(E(V-I))$ for F555W of 1.577 ± 1.100 mag using $R_V = 3.1$. We conclude that the M31 PLR dispersions and slopes by themselves are not reliable due to their dependence on period and position distribution and the effects of high differential extinction. In Figure 3, we do not attempt to fit the PLR. However, we do fit the PLR for the Wesenheit indices in Figure 4, which have slopes very close to those from Riess et al. (2019a), demonstrating the effectiveness of these formulations at removing reddening even in areas of substantial differential extinction.

4. Distance to M31

4.1. NIR Distance Determination

To derive a distance to M31, we first find the relative distance modulus between M31 and the LMC by fitting the m_H^W PLR found here with a fixed slope of -3.26 from Table 3 of Riess et al. (2019a) and subtracting the resulting m_H^W intercept from the m_H^W intercept of 15.915, from Table 5 of Yuan et al. (2020), which corrects the value from Riess et al. (2019a) for CRNL. We then add this relative distance modulus to the most direct and precise geometric distance determination to the LMC available to date of $\mu_0 = 18.477 \pm 0.007$ mag (Pietrzyński et al. 2019) based on detached eclipsing binaries. As Riess et al. (2019a) use the same filters as this study, we do not need to apply further corrections. Due to the wide positional spread of Cepheids over the disk of M31 for our samples, we used the deprojected metallicity gradient of $12 + \log[\text{O}/\text{H}] = 9.10(\pm 0.06) - 0.021(\pm 0.0048)$ dex kpc $^{-1}$ measured by Sanders et al. (2012) from 60 H II regions on the same scale as Zaritsky et al. (1994). These values range from $\log[\text{O}/\text{H}] = 8.72$ to 9.04 and have a mean of 8.85 and a dispersion of 0.06. We adopt a mean metallicity for the LMC of -0.3 dex (relative to 8.9 for solar) used in Riess et al. (2019a), as the mean of -0.33 dex from Romaniello et al. (2008) and -0.27 dex from Choudhury et al. (2016). Using the metallicity term of -0.17 ± 0.06 mag dex $^{-1}$ fit by Riess et al. (2019a), we apply a $+0.04$ mag correction to the distance modulus. We thus find a distance modulus to M31 of $\mu_0 = 24.419 \pm 0.035$ mag ($D = 765 \pm 12$ kpc) for the gold sample, $\mu_0 = 24.332 \pm 0.054$ mag ($D = 735 \pm 18$ kpc) for the silver sample, $\mu_0 = 24.407 \pm 0.032$ mag ($D = 761 \pm 11$ kpc) for the gold+silver sample, and $\mu_0 = 24.414 \pm 0.032$ mag ($D = 763 \pm 11$ kpc) for the gold+silver-1 sample. Although the removal of the outlier Cepheid in gold+silver-1 decreased χ^2_{dof} to the PLR fit, it only changed the final distance by 0.007 mag, well below the final uncertainty. We find that all samples agree to 1σ . The silver sample has a greater final uncertainty than the gold sample primarily due to a smaller sample size. The ratio between the PLR mean uncertainties of the silver and gold samples is given by $\sqrt{42}/\sqrt{13} = 1.80$, which is greater than the ratio between the mean m_H^W magnitude uncertainties of the gold and silver

Table 2
Photometric Results for M31 Cepheids

Cepheid	R.A.	Decl.	Period	F160W	σ	F814W	σ	F555W	σ	m_H^W	σ	m_I^W	σ	Geo. Corr.	Sample
CEPH-10.91809+41.18565	10.918	41.186	55.938	17.002	0.057	18.757	0.057	20.841	0.085	16.213	0.098	16.048	0.170	0.019	Gold
CEPH-11.00794+41.50202	11.008	41.502	22.200	17.997	0.062	18.987	0.057	20.298	0.069	17.507	0.099	17.283	0.159	0.002	Gold
CEPH-11.02407+41.34854	11.024	41.349	17.605	18.245	0.072	19.677	0.100	21.343	0.146	17.617	0.121	17.512	0.298	0.014	Gold
CEPH-11.05340+41.30685	11.053	41.307	10.631	19.141	0.088	20.493	0.223	22.175	0.339	18.507	0.192	18.307	0.676	0.018	Gold
CEPH-11.09119+41.37223	11.091	41.372	13.156	18.615	0.079	19.713	0.168	21.046	0.191	18.116	0.144	17.981	0.460	0.016	Gold

Note. Gold sample errors are calculated by adding the photometric and template errors in quadrature. An intrinsic scatter of 0.069 mag from Riess et al. (2019a) is added to the NIR Wesenheit in quadrature after propagation. Silver sample F555W, F814W, and F160W mean magnitude errors are calculated by adding in quadrature the photometric errors for each epoch and dividing by the square root of the number of epochs used. These errors are propagated into the VIS and NIR Wesenheit indices. We add a random phase error of 0.13 mag from Macri et al. (2015) in the VIS and NIR Wesenheits in quadrature with the propagated uncertainties as well as the intrinsic scatter of 0.069 to the NIR Wesenheit index. Geometric corrections have been added to the VIS and NIR Wesenheits magnitudes in this table.

(This table is available in its entirety in machine-readable form.)

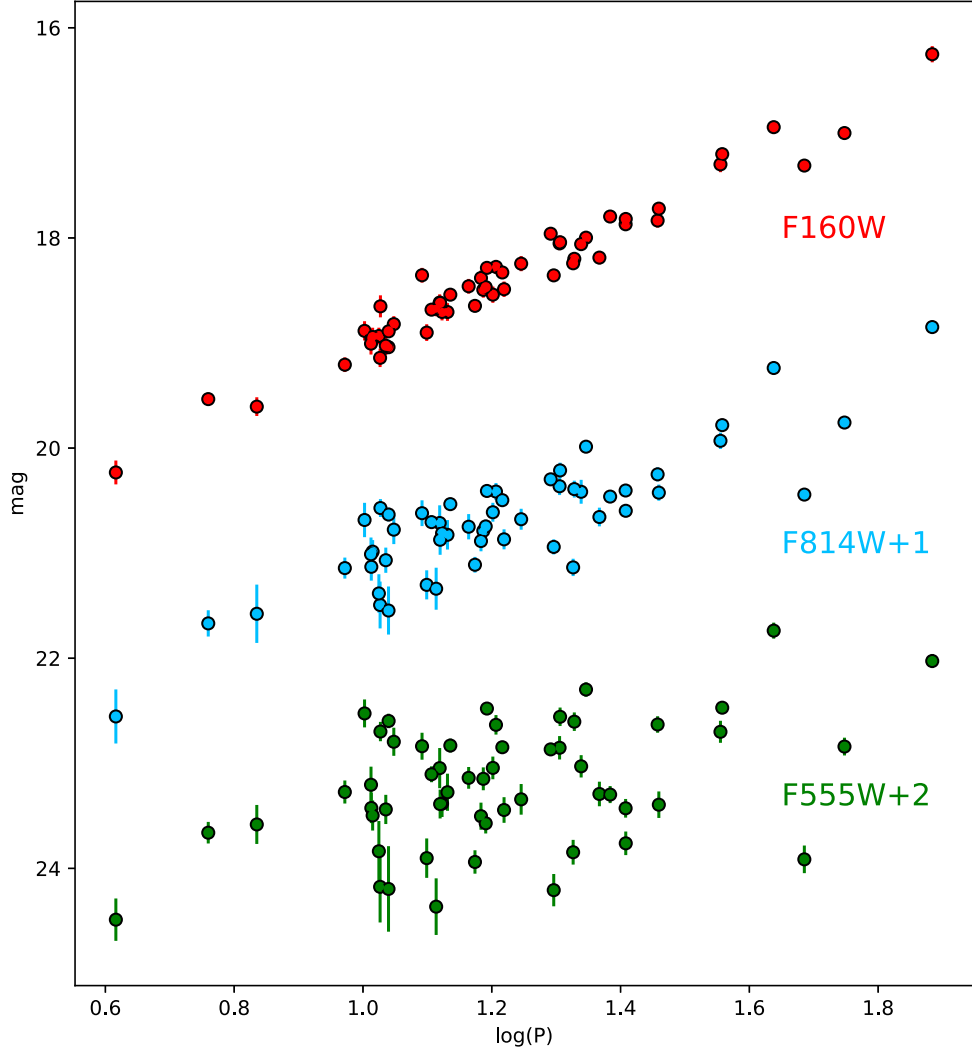


Figure 3. Period-luminosity relations for F555W, F814W, and F160W in the gold+silver sample. Geometric corrections are not applied to F555W, F814W, and F160W in this plot. As explained in Section 3, we do not attempt to fit these PLRs due to high levels of differential extinction making PLRs that are uncorrected for reddening highly unreliable.

samples of 1.31. For the discussion below, we refer only to the distance of the gold+silver sample.

There is an ongoing discussion about the presence of a broken PLR slope at $P = 10$ days (Sandage et al. 2004). Using statistical tests on LMC Cepheids, Ngeow et al. (2008) find a broken slope in the B , V , I_c , J , and H bands, but a linear slope in the K_s and Wesenheit indices. Inno et al. (2013) find linear NIR Wesenheit slopes for LMC Cepheids. Kodric et al. (2018a) find a broken slope for M31 Cepheids in r , i , g , and Wesenheit bands. However, Riess et al. (2016) did not find a broken slope in their m_H^W relation, and Kodric et al. (2018b) did not find a broken PLR slope in any of their samples using 522 fundamental mode Cepheids and 102 first overtone Cepheids in F160W and F110W as well as 559 fundamental mode Cepheids and 111 first overtone Cepheids in F814W and F475W, which is the largest Cepheid sample set compiled to date. To investigate the effect of Cepheids with $P < 10$ days on our distance determination, we removed Cepheids GRP-11.25609+41.56927 (PAndromeda ID: 1068323, period = 6.85 days), GRP-11.03915+41.30692 (PAndromeda ID: 104540, period = 9.362 days), GRP-11.20822+41.44917 (PAndromeda ID: 237868, period = 4.133 days), and GRP-11.24332+41.50926 (PAndromeda ID: 1052211, period = 5.751 days)

from the gold+silver sample. We find that excluding Cepheids with $P < 10$ days decreases the final distance modulus slightly to 24.402 ± 0.033 mag ($D = 759 \pm 11$ kpc) and does not significantly affect our final result.

A breakdown of the error budget for this distance can be found in Table 4. Column (1) lists the type of error, (2) the value of the error in percent, and (3) the source where the error was derived. We combine the error in the M31 PLR mean (0.0169 mag), LMC PLR mean from Riess et al. (2019a) (0.0092 mag), CRNL across 2 dex from Riess et al. (2019b) (0.0013 mag), detached eclipsing binary (DEB) calibration to the LMC from Pietrzynski et al. (2019) (0.0260 mag), and M31 geometry (0.0111 mag) assuming 20% uncertainty. We improve upon past distance determinations to M31 by reducing the total uncertainty to 1.49%, which is the lowest uncertainty published to date that includes anchor uncertainties.

4.2. Comparison with Other Studies

For a historical comparison, our determination agrees to within 1σ with the value of $\mu_0 = 24.33 \pm 0.12$ mag to Baade's field I (3 kpc from the center of M31) from Freedman & Madore (1990). Our distance also agrees with all six mean estimate distances

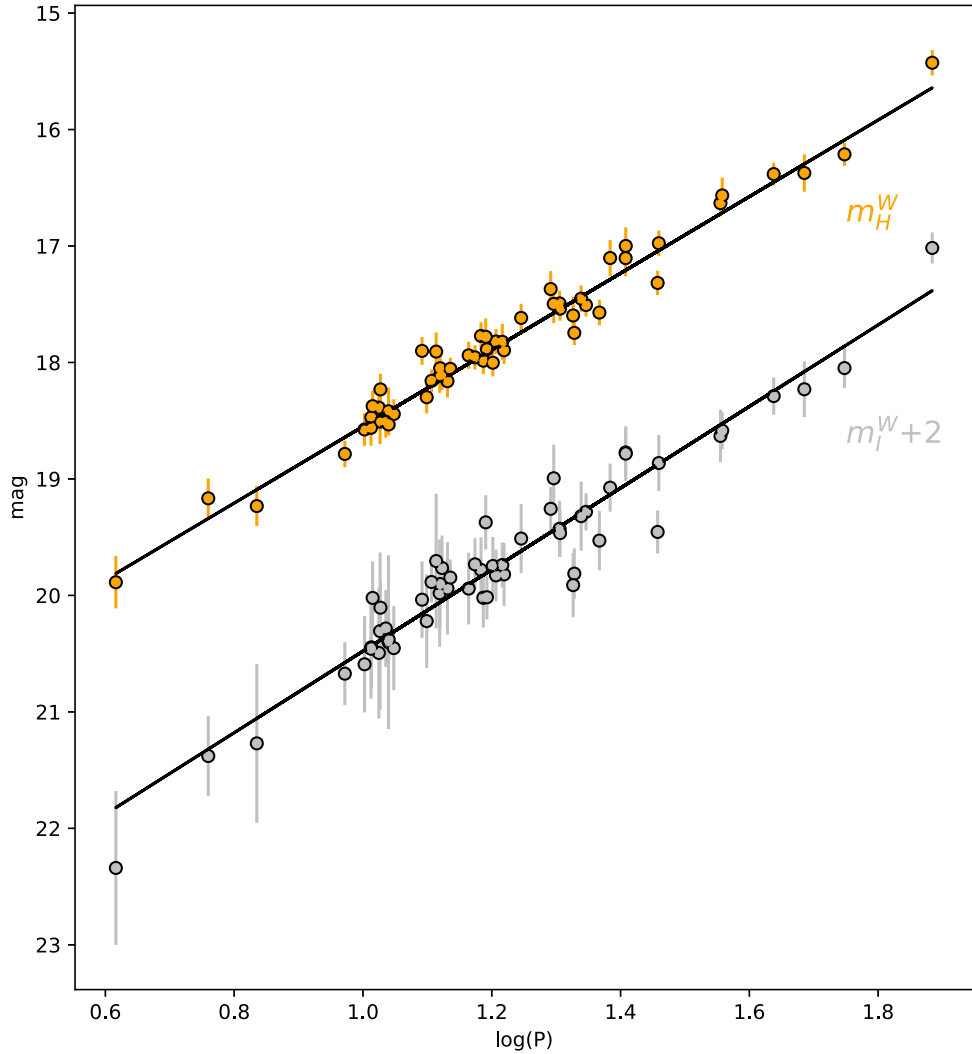


Figure 4. Period–luminosity relations for near-infrared and visible Wesenheit indices in the gold+silver sample. PLR fit parameters can be found in Section 3.

Table 3
Period–Luminosity Relation Fits to HST M31 Cepheids

Index	Sample	N	Dispersion	Slope	Intercept	χ^2_{dof}	Intercept ^a	χ^2_{dof}
m_I^W	Gold	42	0.199	-3.500 (0.144)	21.990 (0.193)	0.892	21.740 (0.038)	0.913
m_H^W	Gold	42	0.132	-3.279 (0.082)	21.838 (0.103)	1.367	21.815 (0.018)	1.335
m_I^W	Silver	13	0.313	-3.486 (0.320)	21.929 (0.433)	1.494	21.693 (0.062)	1.395
m_H^W	Silver	13	0.111	-3.283 (0.181)	21.758 (0.238)	0.537	21.728 (0.045)	0.494
m_I^W	Gold+silver	55	0.231	-3.501 (0.132)	21.980 (0.177)	0.990	21.727 (0.032)	1.011
m_H^W	Gold+silver	55	0.131	-3.289 (0.075)	21.839 (0.095)	1.204	21.803 (0.017)	1.184
m_I^W	Gold+silver-1	54	0.232	-3.506 (0.132)	21.987 (0.178)	0.987	21.728 (0.033)	1.029
m_H^W	Gold+silver-1	54	0.124	-3.311 (0.075)	21.873 (0.095)	1.061	21.809 (0.017)	1.050

Notes. m_H^W includes addition of 0.0154 ± 0.0055 mag to correct for a CRNL of 2 dex between LMC and M31 Cepheids and an intrinsic scatter term of 0.069 from Riess et al. (2019a) added in quadrature to the NIR Wesenheit mean magnitude errors.

^a Linear least-squares fit using a fixed slope of -3.31 for m_I^W and -3.26 for m_H^W , both from Riess et al. (2019a).

(MEDs) (Steer 2020) and the MED for Cepheid distances only of 790 ± 78 kpc from the NASA/IPAC Extragalactic Database (NED) (I. Steer 2020, private communication) as well as the the recommended value of $\mu_0 = 24.45 \pm 0.10$ mag from de Grijs & Bono (2014).

In Table 5, we compare our distance to seven highly cited Cepheid distance measurements to M31 with an uncertainty of less than 10%. We find that our measurement agrees to within

1σ with all originally published measurements except for Saha et al. (2006). However, we note that Saha et al. (2006) used an LMC calibration of $\mu_0 = 18.54$ mag and that updating this calibration with the most direct and precise measurement currently available from Pietrzyński et al. (2019) would lower their distance to $\mu_0 = 24.48$ mag and into agreement with our distance. We combine the H , I , and V distances from Macri et al. (2001) into an m_H^W relation using Equation (1).

Table 4
Systematic Error Budget for Calibration of the M31 Distance Ladder

Error (1)	Value (2)	Source (3)
M31 PLR mean	0.78%	Measured here
LMC PLR mean	0.42%	Riess et al. (2019a)
CRNL across 2 dex	0.06%	Riess et al. (2019b)
LMC DEB mean	1.20%	Pietrzyński et al. (2019)
M31 geometry	0.10%	Measured here
Total	1.49%	

As calibrations typically improve over time, in Table 5 and Figure 5 it is reasonable to recalibrate the seven prior M31 Cepheid distance measurements with more recent measurements of their geometric distance calibration or Cepheid metallicity dependence to provide a more homogeneous comparison. In Table 5, column (1) lists the Cepheid study, (2) the original published distance in the upper row and the distance after recalibration in the lower row, (3) the original anchor galaxy, (4) the original anchor distance and uncertainty in the upper row and the recalibration distance reference (given in the table notes) in the lower row, (5) the original metallicity correction in the upper row and the updated metallicity correction in the lower row, and (6) the original metallicity correction in mag dex^{-1} . We recalibrate the metallicity corrections to match the most recent corrections of $-0.17 \text{ mag dex}^{-1}$ from Riess et al. (2019a) for NIR bands and $-0.24 \text{ mag dex}^{-1}$ from Sakai et al. (2004) for VIS bands, and a metallicity difference of $\log[\text{O}/\text{H}] = 8.85 - 8.60 = 0.25$ between the LMC and M31. For comparison, Figure 5 also includes two TRGB and both eclipsing binary measurements, all of which agree to within 1σ . We also calibrate the two TRGB distances to a common zero-point of $M_{\text{TRGB}} = -4.05$ mag used in Freedman et al. (2019) to compare Cepheid and TRGB distances, discussed further in Section 4.3.

4.3. Cepheid and TRGB Comparison

There is a well-known discrepancy between indirect and direct determinations of the Hubble constant, dubbed the “Hubble tension.” However, there is also a smaller difference between the Cepheid and TRGB determinations, which differ at the 4% level (Freedman et al. 2019; Riess et al. 2021) with $<2\sigma$ significance. The availability of both measures at high precision for M31 allows us to further investigate this difference.

The nearness of M31 and sparseness of TRGB stars necessitates a wide-angle survey of the halo of M31 to produce a precise measure of its TRGB. Unfortunately, the few M31 halo fields observed with HST do not produce a well-sampled, reliable determination of the TRGB. To ensure a meaningful comparison we therefore select ground-based studies that measure the TRGB in the I band or equivalent and satisfy the criterion for a meaningful detection of the TRGB from Madore & Freedman (1995), which requires a minimum number of 100 stars in the bin one magnitude fainter than the identified TRGB. There are two such ground-based studies that satisfy these criteria. McConnachie et al. (2005) used a 40 deg^2 survey with the Isaac Newton Telescope and, assuming $M_I = -4.05$, found $\mu_0 = 24.47 \pm 0.07$ mag. In addition, Conn et al. (2012) used the PAndAS survey undertaken on the Canada–France–Hawaii Telescope and, assuming $M_I = -4.04$ (transformed in

Bellazzini 2008), derived $\mu_0 = 24.46 \pm 0.05$ mag. These results are in good agreement with earlier studies from Sakai et al. (2004) and Ferrarese et al. (2000), both of which result in a lower precision due to sparse color–magnitude diagrams from Mould & Kristian (1986).

In Table 6, we provide the results from McConnachie et al. (2005) and Conn et al. (2012) used to measure distances to M31 from their TRGB determinations. Column (1) lists the TRGB study, (2) the original derived distance modulus μ_0 , (3) the original value of M_I , (4) the assumed extinction, and (5) the change in M_I implied by using the distance derived in this study to recalibrate the TRGB luminosity.

Nominally, the distance to M31 determined here from Cepheids on the HST system in M31 and the LMC and the LMC DEB distance is ~ 0.05 mag closer than the best estimates derived from TRGB with the calibration of $M_I = -4.05$ mag, implying $M_I = -4.00$ mag if we attribute the difference to the TRGB calibration and not chance.⁴ We take a wider view of this difference in Section 5 by including the consideration of other hosts.

4.4. M31 as a Potential Anchor

While there are currently two geometric non-detached eclipsing distances to M31 that could be used to turn M31 into an anchor galaxy, both are from early-type stars (for instance, late O and early B spectral types from Ribas et al. 2005) and rely on non-local thermal equilibrium models that are not strictly geometric and do not yet have a robust grasp on uncertainties. In addition, non-detached eclipsing measurements can be affected by distortion and reflection (Vilardell et al. 2010) that require non-empirical models to correct, and the use of these eclipsing binaries may differ from the use of cooler, late-type stars (de Grijs & Bono 2014). While precise empirical calibrations exist for late-type DEBs (Pietrzyński et al. 2019) and currently hundreds of eclipsing binaries have been discovered in M31 (e.g., Lee et al. 2014), only 11 are bright enough ($V < 20.5$ mag) for radial velocity observations and would require observations with large, 8–10 m ground-based telescopes to obtain radial velocity measurements with suitable signal-to-noise ratios (Beaton et al. 2018). This may be feasible with forthcoming larger telescopes.

In addition, while five water masers have been discovered in M31 by Darling (2011), only two are bright enough for observations with the Very Long Baseline Interferometer and both reside in high-mass star-forming regions that have high noncircular motions, which restrict precision of a geometric distance to $\sim 20\%$ (A. Brunthaler 2021, private communication). A late-type detached eclipsing binary or additional bright water maser measurement in M31 could help tie the Cepheid PLR here to a robust anchor that would allow M31 to be used as a high-precision anchor on par with the MW, LMC, and NGC 4258 and further reduce uncertainty in the Hubble constant by diversifying anchors.

5. Discussion

We construct Cepheid PLRs in M31 in F555W, F814W, and F160W, and construct VIS and NIR Wesenheit indices from

⁴ We would not know how to apply this difference directly to the Cepheid luminosity because we derive the distance to M31 from a direct comparison to LMC Cepheids rather than from an independent determination of Cepheid luminosity.

Table 5
Recalibrated Cepheid Distances

Study	Published μ_0 (Updated)	Anchor	Anchor μ_0 (mag) (Updated)	Metal. Corr. (mag) (Updated) ^a	Metal. Corr. (mag dex ⁻¹)
Macri et al. (2001)	24.44 (0.11) ^{b,c} 24.46 (0.11)	LMC	18.50 (0.10) (1)	0 0.04	0
Freedman et al. (2001)	24.48 (0.05) ^b 24.42 (0.05)	LMC	18.50 (0.10) (1)	0.10 0.06	-0.2
Sakai et al. (2004)	24.38 (0.05) ^b 24.34 (0.05)	LMC	18.50 (0.10) (1)	0.08 ^d 0.06	-0.24 (0.05)
Saha et al. (2006)	24.54 (0.07) ^b 24.38 (0.07)	LMC	18.54 ^e (1)	0.16 0.06	-0.39 (0.03)
Vilardell et al. (2007)	24.32 (0.12) 24.54 (0.10)	LMC	18.42 (0.06) (1)	-0.10 ^f 0.06	-0.25 (0.09)
Riess et al. (2012)	24.38 (0.064) 24.44 (0.06)	MW	-5.86 (0.04) ^g (3)	0 0	0
Wagner-Kaiser et al. (2015)	24.51 (0.08) 24.35 (0.06)	NGC 4258	29.40 (0.06) (2)	0.16 0	0.22 (0.60)
This study	24.41 (0.03)	LMC	(1)		

Notes. (1) $\mu_0(\text{LMC}) = 18.477 \pm 0.007$ mag (Pietrzynski et al. 2019), (2) $\mu_0(\text{NGC 4258}) = 29.397 \pm 0.031$ mag (Reid et al. 2019), (3) $M_H^W = -5.91 \pm 0.022$ mag (Riess et al. 2021).

^a Updated metallicity corrections adopt the most recent corrections of -0.17 mag dex⁻¹ from Riess et al. (2019a) for NIR bands and -0.24 mag dex⁻¹ from Sakai et al. (2004) for VIS bands, and a metallicity difference of $\log[\text{O}/\text{H}] = 8.85 - 8.60 = 0.25$ between the LMC and M31.

^b Anchor error was not included in the original distance measurement.

^c H -, I -, and V -band distances combined into NIR Wesenheit distance using Equation (1).

^d Original metallicity correction was calculated using $\Delta \log[\text{O}/\text{H}] = 8.68 - 8.34 = 0.34$ from Table 4, Column 3.

^e Error not reported in original paper.

^f Metallicity corrections were applied individually to each Cepheid. A table of these corrections was not available, so we estimate the mean correction as the average of -0.15 mag and -0.05 mag as stated in Vilardell et al. (2007), Section 5.2.

^g Absolute magnitude.

these filters. We also improve the uncertainty in the Cepheid distance to M31 to the 1.5% level, providing high-precision groundwork for using M31 as an anchor galaxy in the cosmic distance ladder that is comparable to other anchor galaxies such as the LMC and NGC 4258. Despite the unfortunate degradation of HST Gyro 2 during the GO-15146 program and the loss of several images, we were still able to significantly reduce the uncertainties from past studies by using the same filter system and instrument as our LMC calibration as well as using a sample set located at the front of M31 that reduces crowding.

While not statistically significant, the ~ 0.05 mag difference between TRGB and Cepheids measured in the previous section is in the same direction and similar in size to the 0.059 mag weighted mean offset identified by Freedman et al. (2019) from their comparison of 28 galaxies with Cepheid and TRGB distances, for which the TRGB distances were also calibrated to $M_I = -4.05$ mag. However, Freedman et al. (2019) do not provide the identity of these galaxies, the significance of this difference, or the source of the distance measurements, so we cannot draw strong conclusions from this comparison.

The HST Key Project presented a calibration of TRGB by directly comparing nine hosts of Cepheid and TRGB measurements in Ferrarese et al. (2000) and found $M_I = -3.99 \pm 0.07$ mag assuming an optical Cepheid metallicity correction term of -0.24 mag dex⁻¹ (Sakai et al. 2004), and -4.06 ± 0.07 mag in the absence of a metallicity correction. The same metallicity term was used in the determinations of H_0 by Freedman et al. (2001, 2012). This correction has recently been confirmed to higher precision by Breuval et al. (2021), who found -0.251 ± 0.057 mag dex⁻¹ between the MW, LMC, and the Small Magellanic Cloud (SMC). Kourkchi et al. (2020) also

find a discrepancy between Cepheid and TRGB distance measurements in the same direction, a 0.13 mag disagreement for 25 galaxies. Thus at face value, a concordance between Cepheid and TRGB distances appears to occur at a TRGB calibration of $M_I \sim -4.00$, which is 0.05 mag fainter than the Freedman et al. (2019) calibration. This difference does not appear to depend on distance, and the distance range of the comparison $D < 20$ Mpc is within the range where both methods are well measured.

A fainter calibration of TRGB, $M_I = -3.97 \pm 0.06$ mag, was found by Soltis et al. (2021) from the Gaia EDR3 parallax of ω Cen (which is consistent with Baumgardt et al. 2019; Capozzi & Raffelt 2020; Maíz Apellániz et al. 2021). The size and direction of this difference in calibration is also seen in two recent calibrations of TRGB in the same galaxy, NGC 4258, using the same maser distance by Reid et al. (2019). Jang et al. (2021) find $M_I = -4.05$ and Anand et al. (2021) report $M_I = -3.99$. These studies use different methods to measure the apparent location of the TRGB in NGC 4258. Jang et al. (2021) find an apparent magnitude of $m_{\text{F814W}} = 25.38 \pm 0.02$ using edge detection with a Sobel filter for the same image (GO 9477, ACS) for which the Extragalactic Distance Database (EDD) approach from Anand et al. (2021) using maximum likelihood (fitting a broken luminosity function) yields 25.43 ± 0.03 mag. Differences in the way stars are selected may play a role. The LMC is a more challenging place to refine the calibration of the TRGB due to the presence of significant foreground extinction, which is not present to the same level in the halos of other galaxies where the TRGB is measured. This makes it necessary to estimate and remove the absolute extinction rather than relative extinction, which suffers less bias due to cancellation (Yuan et al. 2019; Freedman et al. 2020;

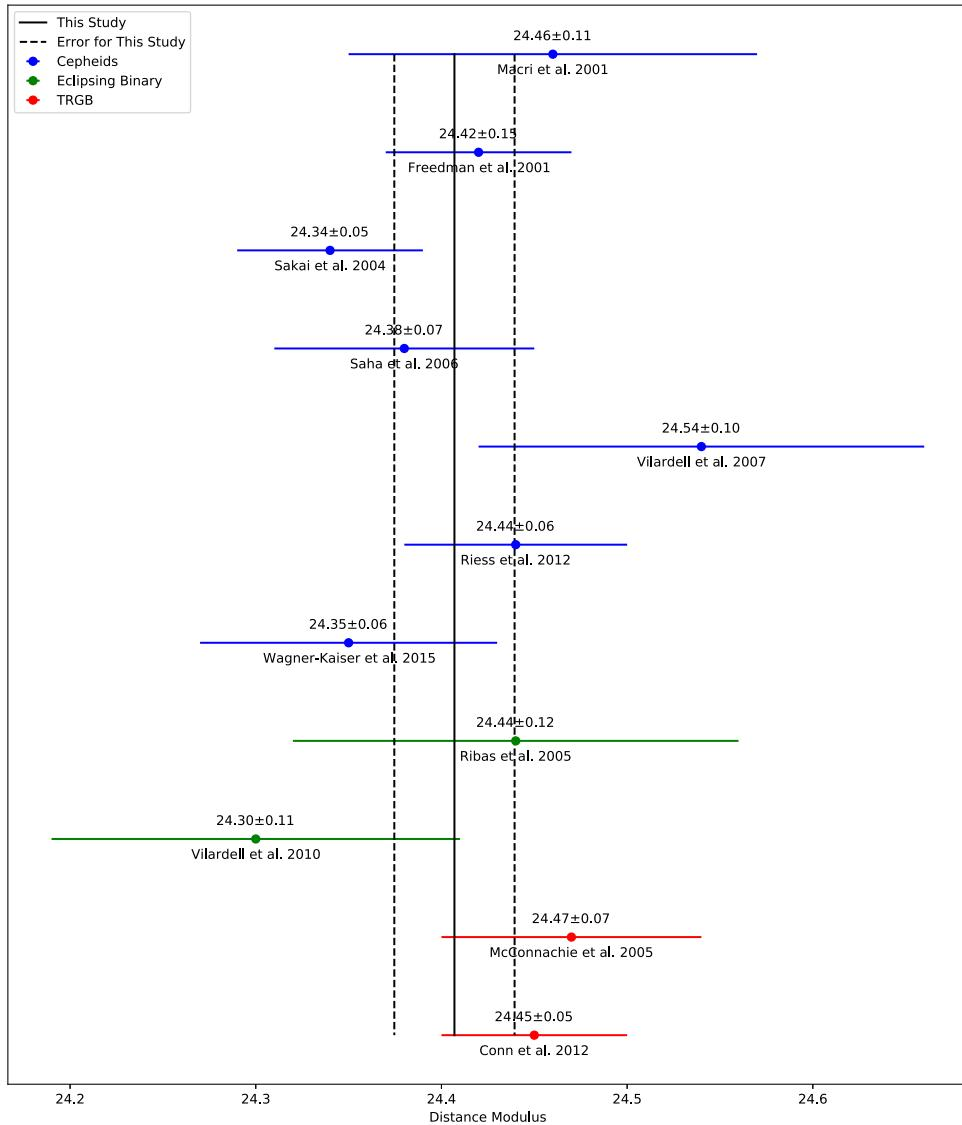


Figure 5. Seven Cepheid, two TRGB, and both eclipsing binary distances to M31. Cepheid measurements were recalibrated using either the DEB distance to the LMC from Pietrzyński et al. (2019) or the water maser distance to NGC 4258 from Reid et al. (2019). TRGB measurements were recalibrated to a zero-point of $M_{\text{TRGB}} = -4.05$ mag. We also update metallicity corrections of $-0.24 \text{ mag dex}^{-1}$ for VIS bands from Sakai et al. (2004) and $-0.17 \text{ mag dex}^{-1}$ for NIR bands from Riess et al. (2019a). We restrict Cepheid distances to those with uncertainties of less than 10%. For TRGB distances, we selected those satisfying the criteria for a robust TRGB detection from Madore & Freedman (1995) and exclude distances to the outer halo or giant stellar stream. The gold+silver distance found here is shown by the vertical black line, with 1σ errors represented by the dashed vertical black lines.

Table 6
Recalibrated TRGB Zero-points

TRGB Study (1)	Original μ_0 (2)	Original M_I (3)	A_I (4)	ΔM_I (5)
McConnachie et al. (2005)	24.47 (0.07)	-4.05 (0.05)	0.12 ^a	0.06
Conn et al. (2012)	24.46 (0.05)	-4.04 (0.12)	0.12 ^a	0.05

Note.

^a Converted from $E(B - V)$ using $R_I = A_I/E(B - V) = 1.94$ from Schlegel et al. (1998).

Nataf et al. 2021). The SMC is also a less ideal laboratory for calibration work due to its large depth. Unfortunately, many of these TRGB and Cepheid comparisons do not use homogeneous data or are not well measured, and no comparison may be individually highly significant, making it hard to resolve this ~ 0.05 mag difference at present. For this reason we have not

revisited these comparisons because their conclusions may not be applicable to present measures. However, this difference in TRGB calibrations, most notably the 0.050 ± 0.036 mag difference in different methods to measure the brightness of the NGC 4258 tip from the same data, which is the simplest to consider because it is independent of all external factors, is of the right size and direction to explain most of the difference in each measurement of H_0 , which is $5 \log(73/70) \sim 0.09$ mag and bears attention.

A clearer resolution may come from new and strong geometric calibrations derived directly from Gaia EDR3 parallaxes. Direct parallaxes of 75 Cepheids from Gaia EDR3 with HST photometry constrain the Cepheid calibration (of SHOES or similarly of the Key Project, neither changed) to 1% in distances (Riess et al. 2021). This calibration from Gaia EDR3 Cepheid parallaxes is supported by prior, independent parallax measurements including those measured with spatial scanning of WFC3 on HST (Riess et al. 2018), with the FGS on

HST (Benedict et al. 2007) or by using Cepheid companions, binary or cluster, (Breuval et al. 2020) in Gaia DR2. An enhanced network of common calibration enabled by Gaia and a growing set of hosts with distance measures with both methods is likely to reduce any remaining discrepancy. In addition, new measurements using these techniques and others with the James Webb Space Telescope may provide improved calibrations.

This research has made use of the NASA/IPAC Extragalactic Database (NED), which is operated by the Jet Propulsion Laboratory, California Institute of Technology, under contract with the National Aeronautics and Space Administration.

M.P.B. is supported by a National Science Foundation Graduate Research Fellowship under grant No. 1746891. M.P.B. thanks the LSSTc Data Science Fellowship Program, which is funded by LSSTc, NSF Cybertraining grant No. 1829740, the Brinson Foundation, and the Moore Foundation; their participation in the program has benefited this work. M.P.B. has been supported by the Director’s Research Fund at STScI.

Support for this work was provided by the National Aeronautics and Space Administration (NASA) through program No. GO-15146 from the Space Telescope Science Institute (STScI), which is operated by AURA, Inc., under NASA contract No. NAS 5-26555. A.G.R., S.C., and L.M.M. gratefully acknowledge support by the Munich Institute for Astro- and Particle Physics (MIAPP) of the DFG cluster of excellence “Origin and Structure of the Universe.”

This research is based primarily on observations with the NASA/ESA Hubble Space Telescope, obtained at STScI, which is operated by AURA, Inc., under NASA contract No. NAS 5-26555.

The HST data used in this paper are available at <https://doi.org/10.17909/t9-epb2-fp05> as part of the MAST archive, which can be accessed at <http://archive.stsci.edu/hst/>.

ORCID iDs

Siyang Li <https://orcid.org/0000-0002-8623-1082>
 Adam G. Riess <https://orcid.org/0000-0002-6124-1196>
 Michael P. Busch <https://orcid.org/0000-0003-4961-6511>
 Lucas M. Macri <https://orcid.org/0000-0002-1775-4859>
 Wenlong Yuan <https://orcid.org/0000-0001-9420-6525>

References

Anand, G. S., Luca, R., Tully, R. B., et al. 2021, *AJ*, **162**, 80
 Baumgardt, H., Hilker, M., Sollima, A., & Bellini, A. 2019, *MNRAS*, **482**, 5138
 Beaton, R. L., Bono, G., Braga, V. F., et al. 2018, *SSRv*, **214**, 113
 Bellazzini, M. 2008, *MmSAI*, **79**, 440
 Benedict, G. F., McArthur, B. E., Feast, M. W., et al. 2007, *AJ*, **133**, 1810
 Bradley, L., Sipócz, B., Robitaille, T., et al. 2020, *astropy/photutils*: 1.0.1, v1.0.1, Zenodo, doi:[10.5281/zenodo.4049061](https://doi.org/10.5281/zenodo.4049061)
 Breuval, L., Kervella, P., Anderson, R. I., et al. 2020, *A&A*, **643**, A115
 Breuval, L., Kervella, P., Wielgórski, P., et al. 2021, *ApJ*, **913**, 38
 Capozzi, F., & Raffelt, G. 2020, *PhRvD*, **102**, 083007
 Cardelli, J. A., Clayton, G. C., & Mathis, J. S. 1989, *ApJ*, **345**, 245
 Choudhury, S., Subramaniam, A., & Cole, A. A. 2016, *MNRAS*, **455**, 1855
 Conn, A. R., Ibata, R. A., Lewis, G. F., et al. 2012, *ApJ*, **758**, 11
 Courteau, S., Widrow, L. M., McDonald, M., et al. 2011, *ApJ*, **739**, 20
 Dalcanton, J. J., Williams, B. F., Lang, D., et al. 2012, *ApJS*, **200**, 18
 Darling, J. 2011, *ApJL*, **732**, L2
 de Grijs, R., & Bono, G. 2014, *AJ*, **148**, 17
 Ferrarese, L., Mould, J. R., Kennicutt, R. C. J., et al. 2000, *ApJ*, **529**, 745
 Fitzpatrick, E. L. 1999, *PASP*, **111**, 63
 Freedman, W. L., & Madore, B. F. 1990, *ApJ*, **365**, 186
 Freedman, W. L., Madore, B. F., Gibson, B. K., et al. 2001, *ApJ*, **553**, 47
 Freedman, W. L., Madore, B. F., Hatt, D., et al. 2019, *ApJ*, **882**, 34
 Freedman, W. L., Madore, B. F., Hoyt, T., et al. 2020, *ApJ*, **891**, 57
 Freedman, W. L., Madore, B. F., Scowcroft, V., et al. 2012, *ApJ*, **758**, 24
 Hubble, E. 1929, *PNAS*, **15**, 168
 Inno, L., Matsunaga, N., Bono, G., et al. 2013, *ApJ*, **764**, 84
 Inno, L., Matsunaga, N., Romanillo, M., et al. 2015, *A&A*, **576**, A30
 Jang, I. S., Hoyt, T. J., Beaton, R. L., et al. 2021, *ApJ*, **906**, 125
 Jones, D. O., Scolnic, D. M., & Rodney, S. A. 2015, PythonPhot: Simple DAOPHOT-type photometry in Python, *Astrophysics Source Code Library*, ascl:[1501.010](https://doi.org/10.5281/zenodo.1501.010)
 Kodric, M., Riffeser, A., Hopp, U., et al. 2018a, *AJ*, **156**, 130
 Kodric, M., Riffeser, A., Seitz, S., et al. 2018b, *ApJ*, **864**, 59
 Kourkchi, E., Tully, R. B., Anand, G. S., et al. 2020, *ApJ*, **896**, 3
 Kozhurina-Platais, V., & Baggett, S. 2020, WFC3 IR Sensitivity Over Time, *Instrument Science Report*, *WFC3 2020-5*
 Leavitt, H. S., & Pickering, E. C. 1912, *HarCi*, **173**, 1
 Lee, C. H., Koppenhoefer, J., Seitz, S., et al. 2014, *ApJ*, **797**, 22
 Macri, L. M., Calzetti, D., Freedman, W. L., et al. 2001, *ApJ*, **549**, 721
 Macri, L. M., Ngeow, C.-C., Kanbur, S. M., Mahzooni, S., & Smitka, M. T. 2015, *AJ*, **149**, 117
 Madore, B. F. 1982, *ApJ*, **253**, 575
 Madore, B. F., & Freedman, W. L. 1991, *PASP*, **103**, 933
 Madore, B. F., & Freedman, W. L. 1995, *AJ*, **109**, 1645
 Maíz Apellániz, J., Pantaleoni González, M., & Barbá, R. H. 2021, *A&A*, **649**, A13
 McConnachie, A. W., Irwin, M. J., Ferguson, A. M. N., et al. 2005, *MNRAS*, **356**, 979
 Mochéjska, B. J., Macri, L. M., Sasselov, D. D., & Stanek, K. Z. 2000, *AJ*, **120**, 810
 Momcheva, I. G., van Dokkum, P. G., van der Wel, A., et al. 2017, *PASP*, **129**, 015004
 Mould, J., & Kristian, J. 1986, *ApJ*, **305**, 591
 Nataf, D. M., Cassisi, S., Casagrande, L., Yuan, W., & Riess, A. G. 2021, *ApJ*, **910**, 121
 Ngeow, C., Kanbur, S. M., & Nanthakumar, A. 2008, *A&A*, **477**, 621
 Pietrzynski, G., Graczyk, D., Gallenne, A., et al. 2019, *Natur*, **567**, 200
 Reid, M. J., Pesce, D. W., & Riess, A. G. 2019, *ApJL*, **886**, L27
 Ribas, I., Jordi, C., Vilardell, F., et al. 2005, *ApJL*, **635**, L37
 Riess, A. G., Casertano, S., Yuan, W., et al. 2018, *ApJ*, **861**, 126
 Riess, A. G., Casertano, S., Yuan, W., et al. 2021, *ApJL*, **908**, L6
 Riess, A. G., Casertano, S., Yuan, W., Macri, L. M., & Scolnic, D. 2019a, *ApJ*, **876**, 85
 Riess, A. G., Fliri, J., & Valls-Gabaud, D. 2012, *ApJ*, **745**, 156
 Riess, A. G., Macri, L., Casertano, S., et al. 2011, *ApJ*, **730**, 119
 Riess, A. G., Macri, L. M., Hoffmann, S. L., et al. 2016, *ApJ*, **826**, 56
 Riess, A. G., Narayan, G., & Calamida, A. 2019b, Calibration of the WFC3-IR Count-rate Nonlinearity, Sub-percent Accuracy for a Factor of a Million in Flux, *Instrument Science Report*, *WFC3 2019-1*
 Romanillo, M., Primas, F., Mottini, M., et al. 2008, *A&A*, **488**, 731
 Saha, A., Thim, F., Tammann, G. A., Reindl, B., & Sandage, A. 2006, *ApJS*, **165**, 108
 Sakai, S., Ferrarese, L., Kennicutt, R. C. J., & Saha, A. 2004, *ApJ*, **608**, 42
 Sandage, A., Tammann, G. A., & Reindl, B. 2004, *A&A*, **424**, 43
 Sanders, N. E., Caldwell, N., McDowell, J., & Harding, P. 2012, *ApJ*, **758**, 133
 Schlegel, D. J., Finkbeiner, D. P., & Davis, M. 1998, *ApJ*, **500**, 525
 Seigar, M. S., Barth, A. J., & Bullock, J. S. 2008, *MNRAS*, **389**, 1911
 Soltis, J., Casertano, S., & Riess, A. G. 2021, *ApJL*, **908**, L5
 Steer, I. 2020, *AJ*, **160**, 199
 Stetson, P. B. 1987, *PASP*, **99**, 191
 Tempel, E., Tamm, A., & Tenjes, P. 2010, *A&A*, **509**, A91
 Vilardell, F., Jordi, C., & Ribas, I. 2007, *A&A*, **473**, 847
 Vilardell, F., Ribas, I., Jordi, C., Fitzpatrick, E. L., & Guinan, E. F. 2010, *A&A*, **509**, A70
 Wagner-Kaiser, R., Sarajedini, A., Dalcanton, J. J., Williams, B. F., & Dolphin, A. 2015, *MNRAS*, **451**, 724
 Walterbos, R. A. M., & Kennicutt, R. C. J. 1988, *A&A*, **198**, 61
 Yoachim, P., McCommas, L. P., Dalcanton, J. J., & Williams, B. F. 2009, *AJ*, **137**, 4697
 Yuan, W., Fausnaugh, M. M., Hoffmann, S. L., et al. 2020, *ApJ*, **902**, 26
 Yuan, W., Riess, A. G., Macri, L. M., Casertano, S., & Scolnic, D. M. 2019, *ApJ*, **886**, 61
 Zaritsky, D., Kennicutt, R. C. J., & Huchra, J. P. 1994, *ApJ*, **420**, 87